

Ruthenium-Modified Bimetallic Zeolitic-Imidazolate Framework Derivative as a High-Efficient Catalyst for Rechargeable Zinc-Air Batteries

Yingying Feng^{+[a]} Haocheng Qi^{+[a]} Qian Zhang^{+[a]} Zhenzhen Chi,^[a] Shuaishuai Zhang,^[a] Yuanyuan Cui,^[c] Shaoliang Li,^[b] Ziyang Guo,^{*[a]} and Lei Wang^{*[a, b]}

Zinc-air (Zn-air) cell has gained lots of attention due to its high specific energy. High activity and good stability of bifunctional electrocatalysts are very critical for Zn-air cell. Herein, Co particles embedded in highly porous N-doping carbon nanocube (Co/HP-NC) has been successfully fabricated by pyrolyzing bimetallic Co/Zn-zeolitic-imidazolate framework (ZIF) and further evenly loaded with metallic Ru nanoparticles to obtain Ru-coated Co/HP-NC (Ru@Co/HP-NC). Benefiting from introduction of Zn, Ru@Co/HP-NC shows the large pore volume, small Co particles, high surface contents of Co₃N and pyridinic/graphitic N. Furthermore, theoretical and experimental results further demonstrate that synergy of Ru coating with Co/HP-NC can

greatly improve the oxygen reduction/evolution reaction (ORR/OER) property of Ru@Co/HP-NC. Furthermore, Ru@Co/HP-NC based Zn-air batteries present the high open circuit potential of 1.4 V, large power density of ~210 mW cm⁻², high discharge capacity (791 mAh g⁻¹) and super-long cycling life (~475 cycles) with small overpotentials (~0.89 V). Notably, flexible Zn-air cell with Ru@Co/HP-NC cathode also displays excellent flexibility and superior cycling stability under different bending conditions. The work provides the simple and reliable way to prepare high-efficient electrocatalysts for high-performance metal-air systems.

1. Introduction

With the serious environmental damage and increasing global energy demand, it is vital to develop the cleaner, more efficient and renewable energy storage and conversion devices to address these issues.^[1–4] In recent years, lithium (Li)-ion battery has been widely used in portable devices (such as laptops and mobile phones) and electric cars, but its further development is hindered by its limited energy density and potential safety problems.^[5–7] As a compelling alternative battery to traditional Li-ion battery, zinc (Zn)-air batteries are becoming popular for the higher specific energy, better safety performance, proper working voltage and lower cost.^[8–10] Currently, primary Zn-air batteries have been successfully commercialized to supply electronic watches, calculators, hearing aids and so on.^[11,12]

However, there are still many technological challenges to be solved before the commercial application of rechargeable Zn-air cells. One of the most serious problems is the sluggish dynamics of oxygen reduction/evolution reaction (ORR/OER) in catalytic electrodes, which dramatically discounts the electrochemical property of Zn-air batteries.^[13–15] Hence, the design of an efficient, affordable, and sustainable dual-function catalyst is very crucial for the secondary Zn-air cells.^[16]

Pt-based or Pd-based materials have excellent ORR catalytic properties, but their high-price and inferior stability seriously impede their application in Zn-air batteries.^[17–20] Subsequently, heteroatom doped carbon-based catalysts (for example, nitrogen doping carbon (NC)) have been well studied in the field of electrocatalysis due to their good ORR performance and porous, earth-abundant and highly conductive properties.^[21] Nevertheless, the OER performance of these reported carbons are often not very good. The supported electro-catalysis strategy can effectively improve the ORR and OER performances of the catalysts.^[20,22,23] Recently, transition metal (TM)-based species/carbon catalysts have caused wide interests in Zn-air batteries on account of their moderate catalytic property for ORR/OER.^[24–31] Among various composites, zeolitic imidazolate frameworks (ZIFs) derivatives are promising candidates for multi-functional electrocatalysts since these derive TM-based phases/porous NC composites which are *in-situ* formed by the conversion of N-containing organic ligands and metal centers in ZIFs can efficiently catalyze the reversible reactions in Zn-air cells.^[32] Nevertheless, it should be noted that the significantly reduced porous channels and aggregated TM-based particles over the high-temperature calcining process will seriously deteriorate the catalytic activity of ZIFs-derived catalysts,

[a] Y. Feng,⁺ H. Qi,⁺ Q. Zhang,⁺ Z. Chi, S. Zhang, Z. Guo, Dr. L. Wang
Key Laboratory of Eco-chemical Engineering
Taishan Scholar Advantage and Characteristic Discipline Team of Eco
Chemical Process and Technology
College of Chemistry and Molecular Engineering
Qingdao University of Science and Technology
Qingdao 266042, China
E-mail: zyguo@qust.edu.cn
inorchemwl@126.com

[b] S. Li, Dr. L. Wang
College of Environment and Safety Engineering
Qingdao University of Science and Technology
Qingdao, Shandong 266042, China

[c] Y. Cui
Shimadzu China Co., Ltd.
Shanghai 200233, China

[†] These authors contributed equally to this work.

Supporting information for this article is available on the WWW under
<https://doi.org/10.1002/batt.202100217>

especially for OER.^[33,34] On the other hand, Ru and Ir containing materials have been proved to be superior electrocatalysts for OER.^[35–38] Therefore, coating Ru or Ir on the ZIF-derived materials with enough pores and highly dispersed TM-based nanoparticles should be the highly desirable procedures to construct the idea bifunctional catalysts.^[39]

Herein, bimetallic Co/Zn-ZIF was synthesized through the seed-mediated method and subsequently pyrolyzed this ZIF at the high-temperature to obtain the Co particles encapsulated in the highly porous N-doped carbon nanocube (Co/HP-NC). The as-prepared Co/HP-NC was further modified with Ru particles on the surface to obtain Ru-coated Co/HP-NC (Ru@Co/HP-NC). The emission of Zn vapors over the high-temperature carbonization process of Co/Zn-ZIF not only obviously enhances the porosity of Co/HP-NC, but also makes the metal nanoparticles highly dispersed in these derivatives. In addition, the contents of the pyridinic/graphitic N and Co₄N are also effectively improved due to the introduction of Zn in the precursors. Moreover, the uniform Ru coating layer greatly increases the surface electrocatalytic activities of Co/HP-NC. Interestingly, the theory calculation/experimental characterizations also are systematically applied to further confirm that the synergy effect of Co/HP-NC and Ru effectively enhance the catalytic performance of Ru@Co/HP-NC. Hence, the Ru@Co/HP-NC exhibits the higher bifunctional catalytic performance than the referenced catalysts (Pt/C and RuO₂). When Ru@Co/HP-NC catalyst has been further investigated in Zn-air system, both the corresponding conventional and flexible batteries also displays the superior electrochemical performances, including the low overpotential, stable voltage curves, long cycling life and so on.

2. Results and Discussion

Figure 1(a) gives a detailed synthetic process of the Ru-coated Co particles encapsulated in the highly porous N-doped carbon nanocube (Ru@Co/HP-NC). As illustrated in Figure 1(a), Co- and Zn-based halide salts react with 2-methylimidazole through the seed-mediated method to synthesize the Co, Zn-based bimetallic zeolitic imidazolate framework (Co/Zn-ZIF). Subsequently, the obtained Co/Zn-ZIF is carbonized at high-temperature during which many pores are formed due to the complete evaporation of Zn vapor and then converted to Co nanoparticles embedded in highly porous N-doping carbon nanocube (Co/HP-NC). After further reacted with RuCl₃, Co/HP-NC is finally uniformly modified with metallic Ru to obtain Ru@Co/HP-NC (see Experimental section for details). To study the morphological characterization of Ru@NC, Ru@Co/HP-NC and Ru@Co/NC and the corresponding precursors, the scanning/transmission electron microscope (SEM/TEM) technologies are conducted. Zn-, Co/Zn- or Co-ZIF samples all show typical cube structures (Figure S1), and their derivatives NC, Co/HP-NC and Co/NC also have the similar nanocube morphology (Figure S2). These results indicate that carbonization does not destroy the basic structure of these ZIFs. Figure 1b and c further present the Ru@Co/HP-NC particles are also the uniform nanocubes

with rough surface, which is also in agreement of the Ru@NC and Ru@Co/NC particles (Figures S3 and S4). These results further indicate Ru-coating layer does not damage the original frame. Besides, the TEM image of Figure 1d shows that a number of Co-based nanoparticles (approximately 3 to 4 nm in diameter) are uniformly embedded into these cubes. From high-resolution (HR) TEM image (Figure 1e-g), three lattice fringes are found in Ru@Co/HP-NC: 0.20, 0.33 and 0.23 nm, assigned to (111) layer of metallic Co, (002) layer of graphitic carbon and (100) plane of metallic Ru.^[40] This phenomenon demonstrates the successful coating of Ru species on Ru@Co/HP-NC. Moreover, the energy-dispersive X-ray (EDX) mapping technology of Ru@Co/HP-NC is studied. The evenly distributed C, N, Co and Ru in the carbon-based framework (Figure 1h-l) confirm the complete volatilization of Zn and the uniformly dispersed Ru in the Ru@Co/HP-NC.

To further analyze crystalline structure of Ru@NC, Ru@Co/HP-NC, Ru@Co/NC and their precursors, their powder X-ray diffraction (XRD) data are measured. XRD results of the precursor Co/Zn-ZIF and Co-ZIF (Figure S5) are approximately consistent with the main peaks of the standard ZIF-67,^[41] indicating the successful preparation of the ZIFs. It can be observed from Figure S6 that there is a broad peak located at around 26° in the three derivatives, which is attributed to graphite.^[42] In addition, there are two obvious peaks located at around 44.2°, 51.5° and 75.8° assigned to the bands of Co (JCPDS No. 15-0806) in the Co/HP-NC and Co/NC.^[43] In the XRD patterns of the Ru@NC, Ru@Co/HP-NC and Ru@Co/NC, apart from the bands assigned to their corresponding precursors, the additional peaks at around 38°, 44°, 58°, or 69° ascribed to metallic Ru can be also observed (Figure 2a). The surface element composition of Ru@NC, Ru@Co/HP-NC and Ru@Co/NC are also analyzed using X-ray photoelectron spectroscopy (XPS) measurement. N, C and Ru species are clearly observed in the overall XPS signal of Ru@NC, Ru@Co/HP-NC (Figure S7). The above phenomenon also suggests the successful introduction of metallic Ru phase in these Ru-based samples. The N1s XPS spectra of Ru@NC, Ru@Co/HP-NC and Ru@Co/NC (Figure 2b) can be resolved into three different N phases: pyridinic N (N-6) at 398.6 eV, pyrrolic N (N-5) at 399.9 eV and graphite N (N-Q) at 401 eV. Recent studies have shown that the existence of (N-6+N-Q) is critical to ORR performance.^[44,45] In Figure 2(c), the (N-6+N-Q) amount on surface of Ru@Co/HP-NC (71.3%) is higher compared with Ru@NC (56.2%) or Ru@Co/NC (60.0%). The Co spectra of three Ru based catalysts (Figure S8) could be divided into four subpeaks: Co-N (782.6 eV), Co²⁺ (780.9 eV), Co (778.4 eV) and satellite phases (786.1 eV).^[46] In addition, Co-N phases have been proved to promote OER property.^[47] In Figure S9, the Co-N phase contents on Ru@Co/NC and Ru@Co/HP-NC surface are 41.4% and 27.9%, respectively. These phenomena indicate the introduction of Zn adjusts the surface type and content of N element. The comparisons of the Ru 3d/C1s XPS data in Ru@NC, Ru@Co/HP-NC and Ru@Co/NC (Figure 2d) further demonstrate the successful formation of metallic Ru in these final samples. It can be calculated from Table S1 that the surface amounts of Ru and Co in Ru@Co/HP-NC are 8.78 wt.% and 1.59 wt.%, respectively, which are

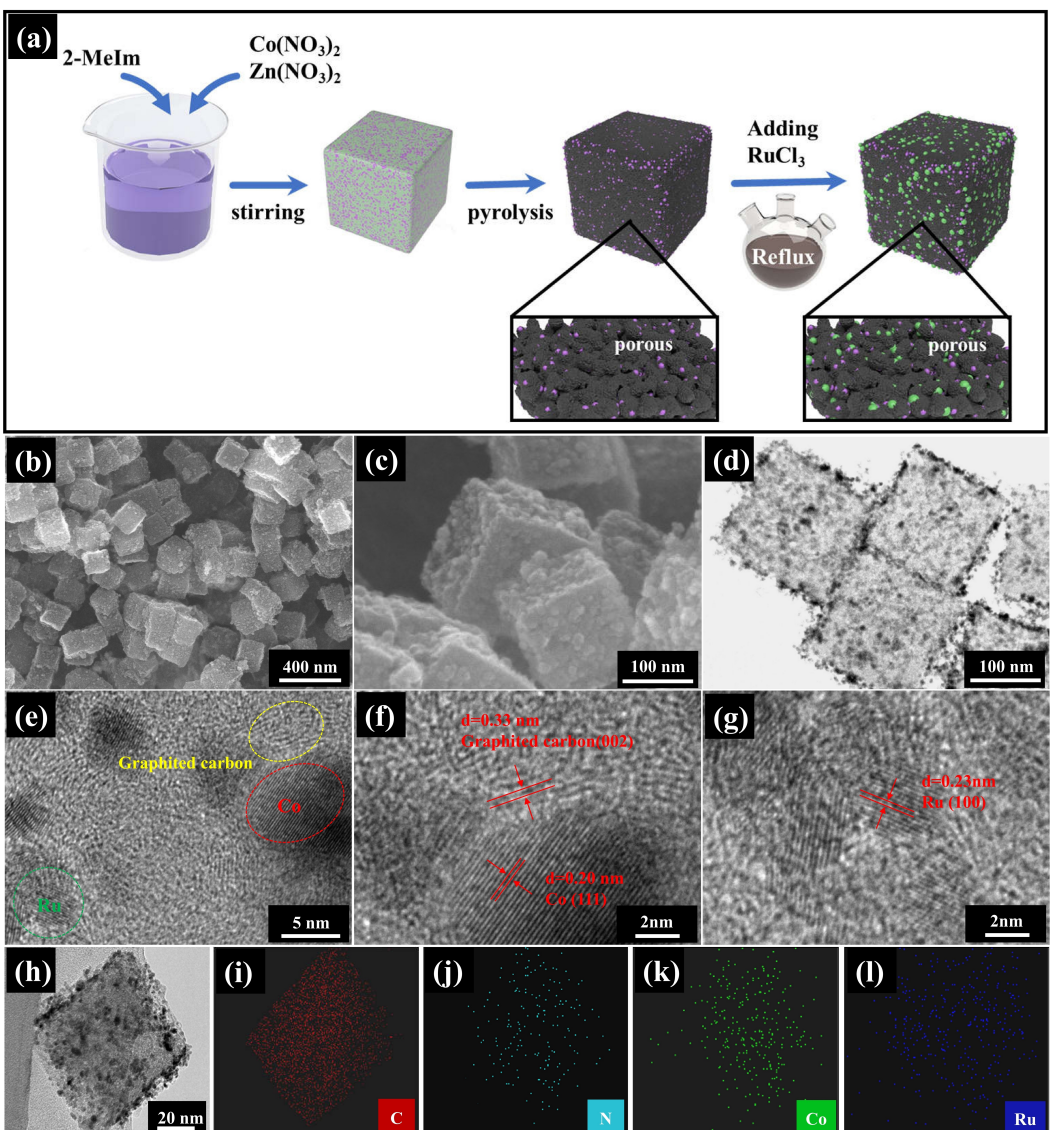


Figure 1. (a) Detailed schematic diagram for synthesis steps of Ru@Co/HP-NC. (b, c) SEM and (d–g) TEM images of Ru@Co/HP-NC. (h–l) EDX mapping characterization of Ru@Co/HP-NC.

beneficial to catalytic performance. These results suggest that the N-doped porous carbon framework in Ru@Co/HP-NC may be the active sites for ORR and Ru and Co–N species should be the active sites towards OER. Moreover, the inductively coupled plasma optical emission spectroscopy (ICP-OES) results shown in Table S2 suggest that the content of Zn element in Ru@Co/HP-NC is very limited and thus can be negligible. The N_2 adsorption measurements of Ru@NC, Ru@Co/NC and Ru@Co/HP-NC are also analyzed to study their pore size distribution (Figure 2e). Ru@Co/HP-NC show apparent hysteretic phenomenon within 0.7–1.0 and an apparently increasing trend at $P/P_0 < 0.05$. In the mean pore size distribution (Figure 2f), there are microporous and mesoporous channels in Ru@Co/HP-NC, Ru@Co/NC and Ru@NC. These results indicate that both micro-pores and mesopores co-exist in all these Ru-based samples. It can be further observed from the Table S3 the pore volume of the Ru@Co/HP-NC ($0.119 \text{ cm}^3 \text{ g}^{-1}$) sample is larger than that of

Ru@Co/NC ($0.084 \text{ cm}^3 \text{ g}^{-1}$) and Ru@NC ($0.054 \text{ cm}^3 \text{ g}^{-1}$), respectively. This result indicates the volatilization of Zn can effectively increase the pores, thus providing a convenient transport process for the O_2 electrochemistry.

The electrocatalytic performance of Ru@Co/HP-NC is tested by cyclic voltammetry (CV) or linear sweep voltammetry (LSV) technologies in KOH electrolyte. Compared with the CV profile of Ru@Co/HP-NC in N_2 -saturated solution, there is a cathode peak for the CV curve of Ru@Co/HP-NC in O_2 -saturated environment, signifying this Ru-based catalyst is active for ORR (Figure 3a). Detailed ORR property of Ru@Co/HP-NC is further investigated by using the rotating-disk electrode (RDE) test (Figure 3b). For comparison, the NC, Ru@NC, Ru@Co/NC and platinum/carbon (Pt/C) have been conducted at the same condition. As shown in Figures 3(b) and S10, Ru@Co/HP-NC catalyst exhibits markedly enhanced half-wave voltage ($E_{1/2}$, 0.81 V) and largest limited current (E_{l} , 6.44 mA cm^{-2}) among

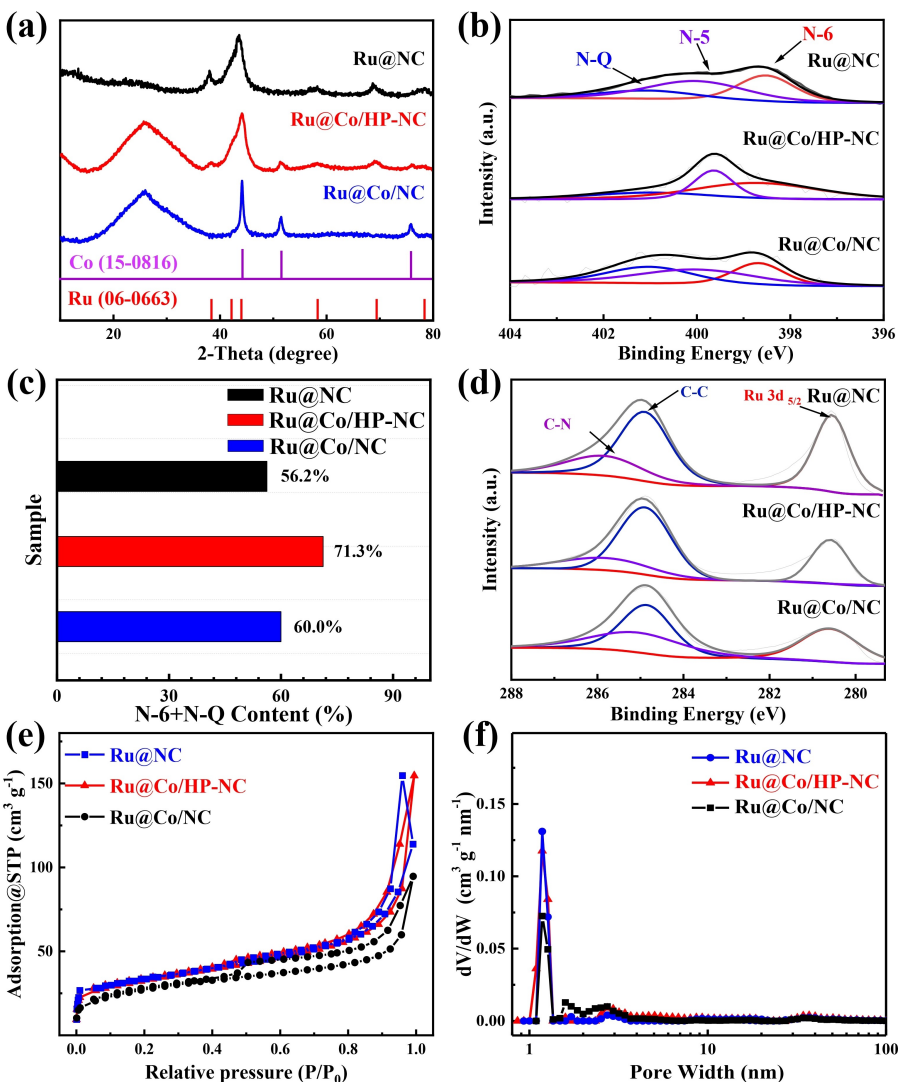


Figure 2. (a) XRD patterns of Ru@NC, Ru@Co/HP-NC and Ru@Co/NC, and their (b) N1s high-resolution XPS spectra, (c) amounts of N-6 and N-Q species, (d) high-resolution C1s/Ru3d XPS spectra, (e) N₂ adsorption/desorption isotherms and (f) pore-size distribution profiles.

these NC-based catalysts, which are comparable to these of Pt/C. The corresponding Tafel plots for all these Ru-coated materials and Pt/C catalyst are also studied (Figure 3c). The Ru@Co/HP-NC presents the slope of 57.9 mVdec⁻¹, which is lower compared with benchmark Pt/C (62.7 mVdec⁻¹) and other catalysts [Ru@Co/NC (93.6 mVdec⁻¹), Ru@NC (148.2 mVdec⁻¹) and NC (149.4 mVdec⁻¹)], indicating fastest ORR kinetics of Ru@Co/HP-NC. The ORR reaction pathways of Ru@Co/NC, Ru@Co/HP-NC and Pt/C catalysts are monitored by measuring electron transfer numbers (*n*) and yield of H₂O₂ by applying rotating ring-disk electrode (RRDE) measurement. Among these catalysts, Ru@Co/HP-NC exhibits the optimal total electron transfer numbers (*n*=3.99) and the lowest H₂O₂ yield of less than 5% (Figure 3d). These results suggest that Ru@Co/HP-NC prefers the four-electron oxygen reduction process in which the adsorbed O₂ molecules are directly and effectively reduced. Subsequently, durability tests of Ru@Co/HP-NC and Pt/C catalysts are also estimated by chronoamperometry. As shown in Figure 3(e), there is a stable electrocatalytic activity

with retention of 90.2% in Ru@Co/HP-NC after 31000 s, which is more stable than the Pt/C (only 62.3% retention) and several recently reported catalysts (Table S4). This phenomenon suggests the superior durability of Ru@Co/HP-NC in alkaline electrolytes. After adding 5% methanol (Figure 3f), Ru@Co/HP-NC exhibits a negligible current decay, which is also smaller than Pt/C and some catalysts in recent works (Table S5). This result indicates that Ru@Co/HP-NC exhibits super-high methanol tolerance. On the other hand, the OER activity of NC, Ru@NC, Ru@Co/HP-NC, Ru@Co/NC and RuO₂ catalysts are also tested by LSV in KOH electrolyte (1 M). Figure 3(g) presents that voltage hysteresis (versus standard O₂/H₂O equilibrium (1.23 V)) of Ru@Co/HP-NC is 0.26 V, significantly smaller than these of commercial RuO₂ catalysts and other NC-based catalysts at 10 mAcm⁻². Furthermore, Tafel plots of all these Ru-coated materials and RuO₂ catalyst for OER are also studied (Figure 3h). Specifically, the Tafel slope of Ru@Co/HP-NC electrode (95.2 mVdec⁻¹) is much lower compared with NC, Ru@NC, Ru@Co/NC and RuO₂, suggesting the favorable OER perform-

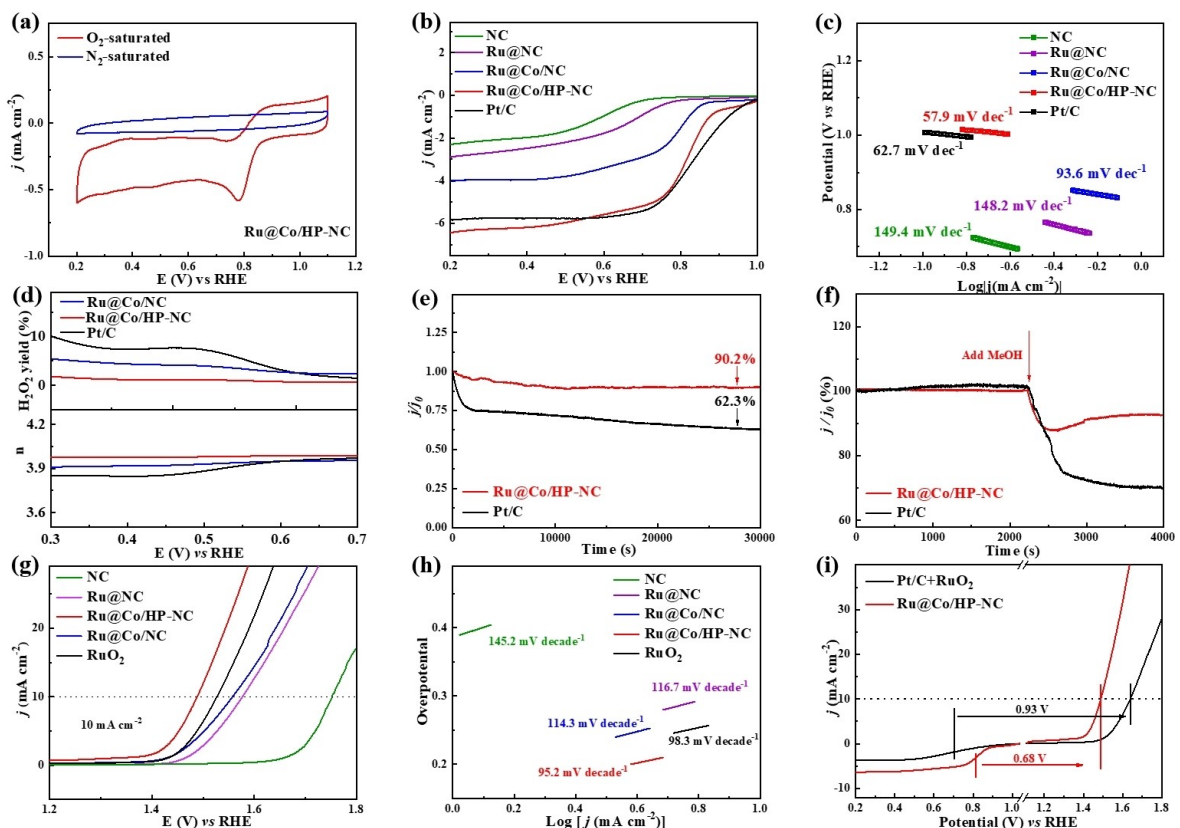


Figure 3. (a) CVs of Ru@Co/HP-NC in the KOH solution (0.1 M) saturated with O₂ or N₂; (b) LSV profiles of Ru@NC, Ru@Co/HP-NC, Ru@Co/NC and platinum carbon (Pt/C) for ORR under the sweep rate of 5 mV s⁻¹ with 1600 rpm, and (c) Tafel plots which is calculated based on ORR curves. (d) Electron transfer numbers and H₂O₂ yield of Ru@NC, Ru@Co/HP-NC, Ru@Co/NC and Pt/C. (e) Chronoamperometric characteristic of Ru@Co/HP-NC and Pt/C under the constant voltage (0.8 V vs. RHE). (f) Methanol toxicity tolerance tests of the Ru@Co/HP-NC and Pt/C by injecting 5 % volume of methanol into the electrolyte. (g) OER properties of Ru@NC, Ru@Co/HP-NC, Ru@Co/NC and RuO₂ with 5 mV s⁻¹, and (h) Tafel curves which are calculated based on OER data. (i) Potential gap (ΔE) of Ru@Co/HP-NC and Pt/C + RuO₂. Scan rate, 5 mV s⁻¹.

ance on Ru@Co/HP-NC. Meanwhile, XPS characterization on the Ru@Co/HP-NC before and after the OER measurement confirm that the metallic Ru was partially oxidized to Ru⁴⁺ after the OER test (Figure S11). In general, the potential difference (ΔE) of $E_{1/2}$ and $E_{j=10}$ ($E_{1/2}$ is half-wave voltage of ORR, while $E_{j=10}$ is OER voltage obtained under 10 mA cm⁻²) has been used to evaluate the overall bifunctional oxygen electrocatalysts. Figure 3(i) shows that ΔE of Ru@Co/HP-NC (0.68 V) greatly outperforms Pt/C + RuO₂ (0.93 V), suggesting its superb catalytic performance.

The first-principle density functional theory (DFT) calculations have also been applied to explore the mechanism of superior ORR/OER performance of Ru@Co/HP-NC. Firstly, we have used theoretical calculations to prove whether there is synergistic effect between Ru and Co/HP-NC in Ru@Co/HP-NC. To simplify the model and facilitate theoretical calculation, the effect of Co particles is not considered in this model since Co particles exist in both Ru@Co/HP-NC and Co/HP-NC which will not change the relative value of the energy barriers. Hence, structures of Co-N₄ doped graphene without/with Ru₈ cluster coating (CoN₄/G and Ru@CoN₄/G) have been constructed as model of Co/HP-NC and Ru@Co/HP-NC in our DFT calculations. Figure 4(a) shows the favorable adsorption sites of various reaction intermediate species on the CoN₄ sites of CoN₄-based

graphene (CoN₄/G) and Ru particles modified CoN₄/G (Ru-CoN₄/G). The calculated free energy diagram of the CoN₄/G and Ru-CoN₄/G catalysts towards ORR and OER is also systematically investigated under different potentials (U) (Figure 4b and c). As shown in Figure 4(b), when $U=0$ V, all the ORR steps on the CoN₄ sites of Ru@CoN₄/G or CoN₄/G are downhill. In the OER process, the sub-reaction step from OH* to O* is the rate-determining step for both catalysts. The energy barrier with Ru@CoN₄/G catalyst is 1.56 eV, which is obviously decreased compared with the CoN₄/G catalyst (1.88 eV). At $U=1.23$ V, according to the calculation results, the forth step (OH* + 3OH⁻ + e⁻ → 4OH⁻) is the rate-limiting step of Ru@CoN₄/G or CoN₄/G over the whole ORR process (Figure 4c). Therefore, the energy barrier of the ORR process at $U=1.23$ V with Ru-CoN₄/G catalyst is 0.36 eV (Figure 4c), which is slightly lower than that with CoN₄/G catalyst (0.43 eV). Impressively, over the OER process, the energy barrier of the rate-determining step OH* + 3OH⁻ + e⁻ → O* + H₂O + 2OH⁻ + 2e⁻ is strongly decreased from 0.64 eV the CoN₄ sites of CoN₄/G to 0.33 eV on the CoN₄ sites of Ru@CoN₄/G. However, the encapsulated/exposed Co nanoparticles and Ru sites of Ru@CoN₄ have been demonstrated to have the blocking effect on the ORR/OER performance (Figures S12 and S13). Although our DFT data indicate that the oxidized Ru is good for OER process, the largest energy

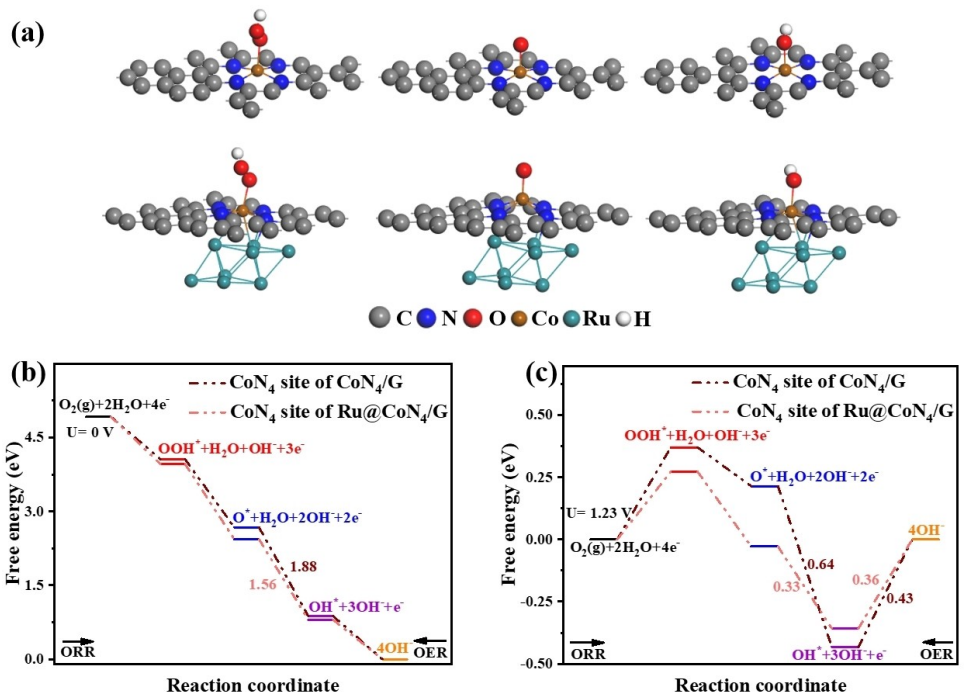


Figure 4. (a) The favorable adsorption sites of various reaction intermediate species on the Co particles embedded in CoN₄-based graphene (Co–CoN₄/G) and Ru modified Co–CoN₄/G (Ru@Co–CoN₄/G). The detailed ORR/OER free energy paths on the CoN₄/G and Ru@CoN₄/G models under (b) $U = 0$ V and (c) $U = 1.23$ V.

barrier on the CoN₄ sites of Ru@CoN₄ over OER process is still lower than these on the oxidized Ru (Figure S14). These theoretical data suggest that the synergistic effect between Ru species and Co/HP-NC can greatly improve the ORR/OER performance, which is in agreement with the detailed experimental results shown in Figure S15.

Inspired by the excellent catalytic properties Ru@Co/HP-NC, a homemade Zn-air battery composed of metallic Zn anode, KOH based electrolyte and Ru@Co/HP-NC cathode is fabricated. In open circuit voltage (OCV) test, the Ru@Co/HP-NC based Zn-air cell has the stable OCV (~1.4 V) for 1440 min (Figure 5a). Figure 5(b) presents the discharge polarization of Ru@Co/HP-NC and Pt/C+RuO₂ mixture (which are mechanically mixed with the mass ratio of 1:1). As revealed in Figure 4(b), the maximum power density of the cell using Ru@Co/HP-NC (210 mW cm⁻²) is higher compared with Pt/C+RuO₂ (103 mW cm⁻²). This further indicates Ru@Co/HP-NC has excellent ORR catalytic activity. Additionally, the mechanical recharging experiments are also carried out (replaced with new Zn film/KOH solution after each discharge for 24 h). At 5 mA cm⁻², the Ru@Co/HP-NC cathodes can still maintain the discharge potential of 1.3 V after 11 times cycles (Figure 5c). Additionally, the specific capacity of Ru@Co/HP-NC cathode is 791 mAh g_{Zn}⁻¹ under current of 5 mA cm⁻², which surpasses the specific capacity of Pt/C+RuO₂ (635 mAh g_{Zn}⁻¹) and most of the recently reported catalysts (Figure 5d and Table S6). Moreover, the specific capacity of Ru@Co/HP-NC based Zn-air cell can still reach to 650 mAh g_{Zn}⁻¹ at 15 mA cm⁻², which indicates that Ru@Co/HP-NC has superior rate performance.

To further explore the potential application of Ru@Co/HP-NC, Zn-air batteries using Ru@Co/HP-NC is also assembled for rechargeable property testing (Figure 6a). Figure 6(b) gives the polarization curves of Zn-air cell using Ru@Co/HP-NC or (Pt/C+RuO₂) at different currents. Voltage gap between the discharge loss and charging rise of Zn-air cell using Ru@Co/HP-NC (0.90 V) is much lower compared with that of the commercial reference (1.12 V) at 100 mA cm⁻², indicating that Ru@Co/HP-NC has a better catalytic reversibility. Figure 6(c) presents the discharge/charge profiles of Ru@Co/HP-NC cathode at 5 mA cm⁻² with 2 h per cycle. This Zn-air battery maintains the stable voltage curves without limited overpotentials (~0.7 V) over the continuous test of 160 h. Even when the test condition is the higher current of 10 mA cm⁻² with the cycling time of 20 min (Figure 6d), Ru@Co/HP-NC electrode still exhibits the better cycling life (> 9500 min) with lower voltage polarization (~0.89 V) than the contrast (Pt/C+RuO₂) catalyst (~6000 min with overpotentials of ~1.13 V) and most of the catalysts in recent work (Table S7). These results reveal the excellent OER/ORR property of Ru@Co/HP-NC in Zn-air batteries.

To further study the possible applicability of Ru@Co/HP-NC in wearable electronic devices, we used the Ru@Co/HP-NC coated carbon cloth, Zn foil and alkaline electrolyte to construct a flexible Zn-air cell (Figure 7a). Zn foil anode and Ru@Co/HP-NC based electrodes exhibit superior flexibility at different bending conditions. As expected, the Zn-air cell with Ru@Co/HP-NC cathode could keep stable OCV at about 1.33 V with the continuous bending operation (Figure 7b). Additionally, the Ru@Co/HP-NC based flexible battery also shows the stable discharge voltage (~1.25 V) for 540 min at 1 mA cm⁻²

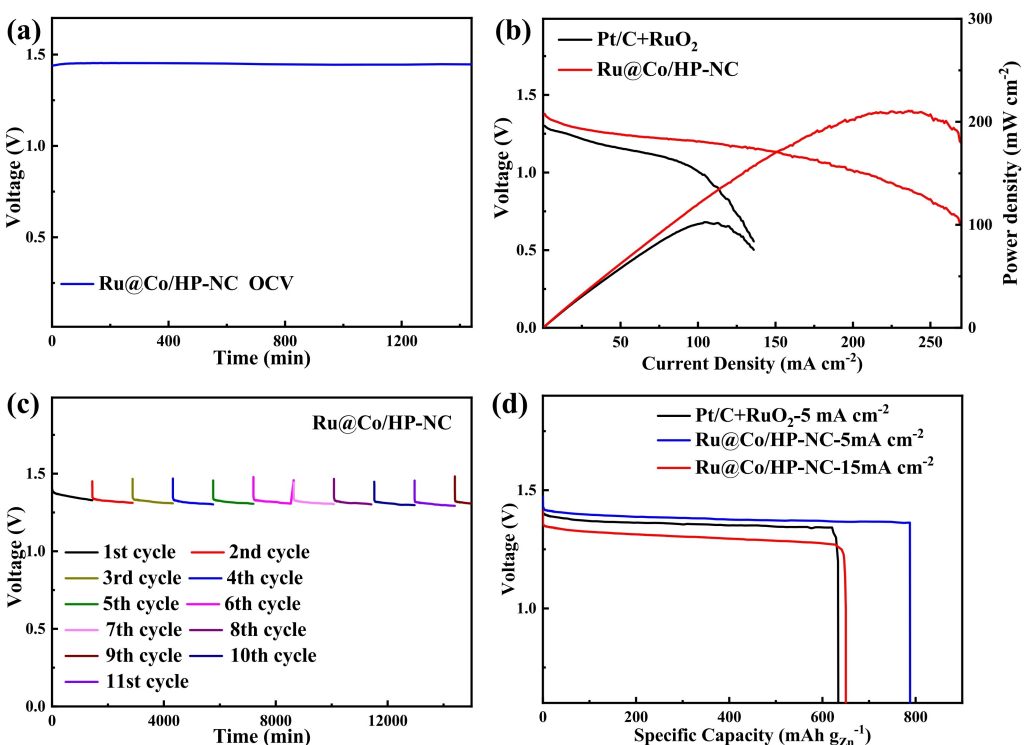


Figure 5. (a) Open-circuit voltage profile for primary Zn-air cell using Ru@Co/HP-NC. (b) Power density and polarization plots for Zn-air cells using Ru@Co/HP-NC or (Pt/C + RuO₂) cathodes. (c) Voltage curve of the Zn-air cell containing Ru@Co/HP-NC electrode by the continuous mechanical charging. (d) The long-term discharge curves for the Zn-air battery containing Ru@Co/HP-NC or (Pt/C + RuO₂) cathodes at 5 mA cm⁻² and 15 mA cm⁻², respectively.

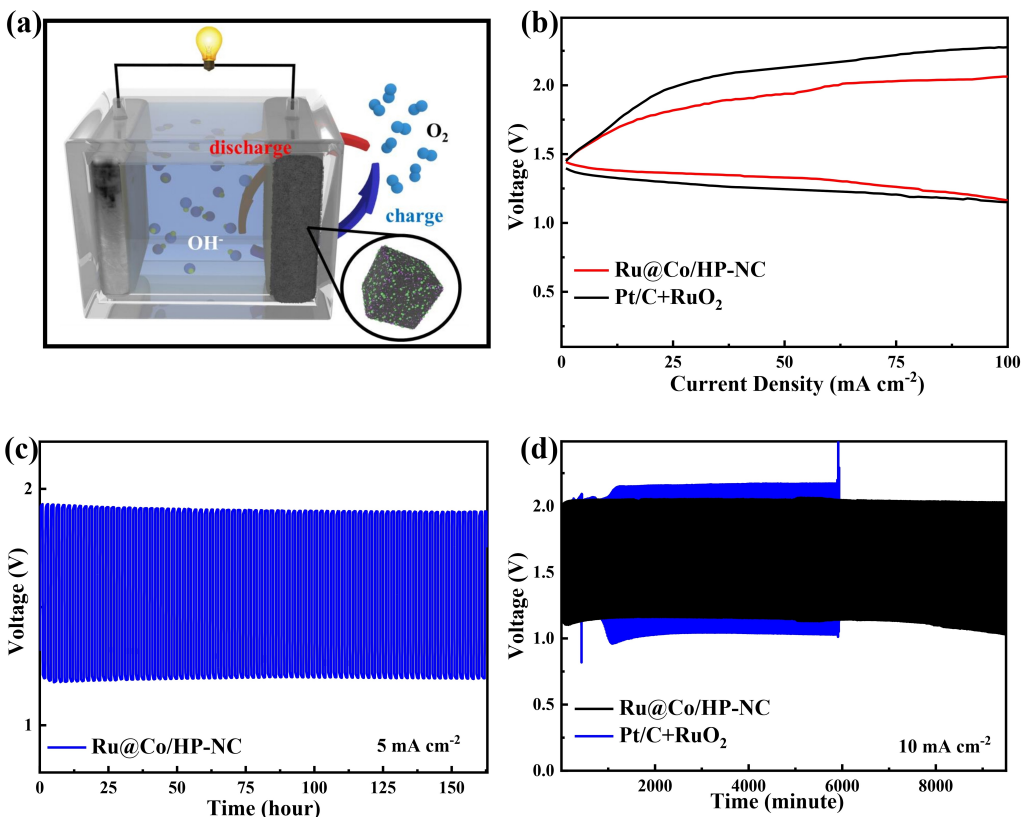


Figure 6. (a) The schematic image of the secondary Zn-air cell. (b) Voltage polarization of Zn-air cells with Ru@Co/HP-NC and Pt/C electrodes. (c) The voltage curves of the rechargeable Zn-air battery with Ru@Co/HP-NC at the current of 5 mA cm⁻² for 2 h every cycle. (d) Cycling tests of Zn-air batteries with Ru@Co/HP-NC or (Pt/C + RuO₂) at 10 mA cm⁻² with 20 min every cycle.

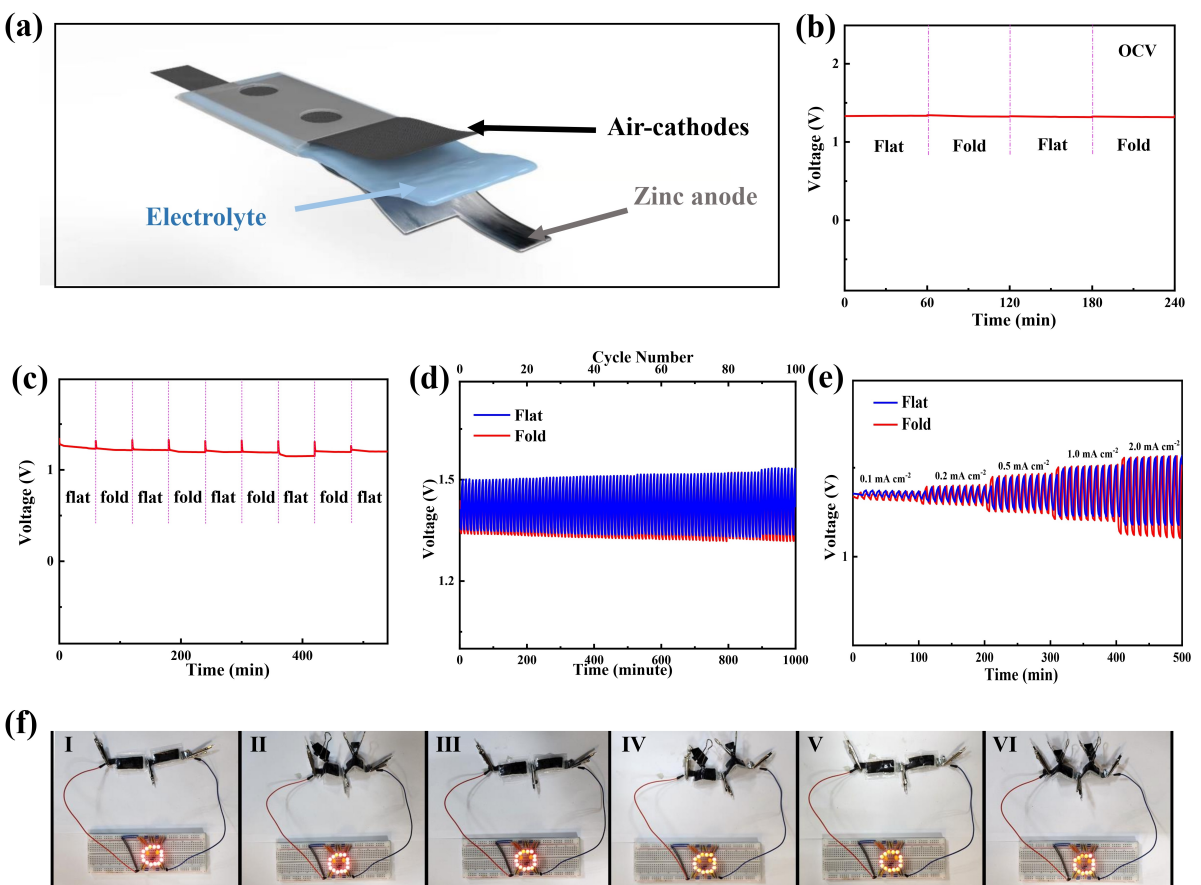


Figure 7. (a) Schematic image of flexible Zn-air cell based on Ru@Co/HP-NC. (b) Open circuit potential of this type battery at a sequence of bending conditions. (c) Discharge profile at 1.0 mA cm^{-2} with 600 s per cycle at various bending stages, (d) cycling performance at 1.0 mA cm^{-2} under flat and fold states and (e) voltage curves of at various currents (from 0.1 to 2.0 mA cm^{-2}) in the flat and fold states for Zn-air battery with Ru@Co/HP-NC cathode. (f) Photographs of LED bulbs which are lightened by two Ru@Co/HP-NC-based flexible Zn-air cells in series under continuous mechanical bending conditions.

under continuous flat and folded conditions (Figure 7c). The above tests reveal the good ORR property of Ru@Co/HP-NC in the flexible cells. Figure 7(d) gives the cycling profiles of Ru@Co/HP-NC based flexible battery at various bending states under 1 mA cm^{-2} . As shown in Figure 7(d), the discharge/charge profiles of this flexible battery under no-bending state are very similar to the cell under bending to 90° over 100 cycles. Additionally, the discharge/charge profiles of these flexible batteries are also very stable with the low average overpotentials of $\sim 0.18 \text{ V}$ over the whole cycling. Moreover, the cycling performance of Ru@Co/HP-NC based flexible battery is much better than that of Pt/C + RuO₂ based flexible (Figure S16), highlighting the superior catalytic performance of Ru@Co/HP-NC. Both voltage curves for flexible Zn-air cells with Ru@Co/HP-NC cathodes under flat and bent conditions are almost reproduced at different currents of $0.25\text{--}2 \text{ mA cm}^{-2}$ (Figure 7e). More interestingly, 16 small light-emitting diodes (LED) have been lighted by two flexible batteries in series even under different bending conditions (Figure 7f). These phenomena suggest the application of Ru@Co/HP-NC in flexible devices is very valuable.

3. Conclusions

In summary, Ru@Co/HP-NC is prepared by the pyrolysis of Co, Zn-based bimetal ZIFs and subsequently Ru nanoparticles coating. The introduction of Zn reduces particle size of metallic Co and optimizes the surface distribution of N species, while its volatilization at high-temperature also increases pore volume in Ru@Co/HP-NC. Additionally, the uniform Ru coating layer further enhances the catalytic activity of Ru@Co/HP-NC. Moreover, theoretical/experimental data confirm that the synergistic effect between Ru species and Co/HP-NC can greatly improve catalytic activity of Ru@Co/HP-NC. Benefiting from the above advantages, the Ru@Co/HP-NC exhibits outstanding bifunctional ORR/OER performance. As a result, the Zn-air battery using Ru@Co/HP-NC cathode exhibits the satisfactory capacity ($791 \text{ mAh g}_{\text{Zn}}^{-1}$), large peak power density ($\sim 21 \text{ mW cm}^{-2}$) and small voltage polarization of 0.89 V and super-long cycling life (~ 475 cycles). More importantly, flexible Ru@Co/HP-NC based Zn-air cell displays excellent cyclic stability and stable discharge profiles even under different bending conditions. This strategy gains a new perspective for high-efficient catalyst design in Zn-air batteries.

Experimental Section

Preparation of Co/HP-NC

Typically, 72.76 mg $\text{Co}(\text{NO}_3)_2 \cdot 6\text{H}_2\text{O}$, $\text{Zn}(\text{NO}_3)_2 \cdot 6\text{H}_2\text{O}$ (223.12 mg) and Cetyltrimethylammonium bromide (CTAB, 5 mg) were mixed into deionized (DI) water (10 mL) by ultrasonic treatment. The above mixture was then quickly injected in 70 mL of DI water containing 4540 mg of 2-methylimidazole (2-Melm) under the magnetic stirring. After stirring for 20 min, the above solution was incubated at 25 °C for 24 h without moving. Then, the solid substance was collected by repeated washing and centrifugation for 5–6 times (using water and ethanol with the volume ratio of 1:1). After that, the residual sample was dried under vacuum. The as-prepared powder was named Co/Zn-ZIF and the molar ratio of Co/Zn is 1/3. Co/Zn-ZIF was calcined under 900 °C in N_2 with 2 h to form the Co particles encapsulated in the highly porous N-doped carbon nanocube (denoted as Co/HP-NC). For comparison, pure Co-ZIF, pure Zn-ZIF and their derivatives (Co embedded into N-doping carbon nanocube (Co/NC) and N-doped carbon nanocube (NC)) were also synthesized at the similar method. The corresponding preparations of these referenced samples were given in the Supporting Information.

Preparation of Ru@Co/HP-NC

Typically, Co/HP-NC (80 mg) was dissolved in ethylene glycol (100 mL) containing $\text{RuCl}_3 \cdot x\text{H}_2\text{O}$ (50 mg). After that, the mixed solution was refluxed in the oil bath (~170 °C) for 3 h. Then the supernatant was removed and the residual material was centrifuged. The obtained was transferred to vacuum oven to dry at 60 °C overnight. Finally, Ru nanoparticles coated Co/HP-NC (Ru@Co/HP-NC) was obtained. Moreover, Ru nanoparticles coated Co/NC (Ru@Co/NC) and Ru nanoparticles coated NC (Ru@NC) were also prepared at the same method for comparison.

Construction of Zn-air batteries and electrochemical measurements

Zn-air cells using above catalysts were assembled to evaluate their performance. Polished zinc strip and 6 M KOH was acted as anode and electrolyte in the cells, respectively. Water-proof and Ru@Co/HP-NC layers were pressed successively with foam nickel as cathode (The detailed preparation is given in the Supporting Information). Battery assembly was performed in air. All data was obtained from the as-fabricated cell with LAND cycler (Wuhan Land Electronic Co. Ltd).

Supporting Information

Supporting Information is available from the Wiley Online Library or from the author.

Acknowledgements

The authors acknowledge funding support from the National Natural Science Foundation of China (21905151 and 51772162), Youth Innovation and Technology Foundation of Shandong Higher Education Institutions, China (2019KJC004), Outstanding Youth Foundation of Shandong Province, China (ZR2019JQ14), Taishan Scholar Young Talent Program, Major Scientific and

Technological Innovation Project (2019JZZY020405), the Postdoctoral Science Foundation of China (2019M652499) and the Postdoctoral Innovation Project of Shandong Province (201903021).

Conflict of Interest

The authors declare no conflict of interest.

Keywords: bimetallic zeolitic-imidazolate framework • flexible electrode • nitrogen-doped carbon • Ru modification • Zn-air batteries

- [1] Z. P. Cano, D. Banham, S. Y. Ye, A. Hintennach, J. Lu, M. Fowle, Z. W. Chen, *Nat. Energy* **2018**, *3*, 279–289.
- [2] D. D. Li, S. S. Zhang, Q. Zhang, P. Kaghazchi, H. C. Qi, J. Liu, Z. Y. Guo, L. Wang, Y. G. Wang, *Energy Storage Mater.* **2020**, *26*, 593–603.
- [3] L. S. Wang, M. H. Jia, X. X. Xu, Q. Wang, *J. Power Sources* **2019**, *437*, 226892.
- [4] Z. Y. Guo, F. M. Wang, Y. Xia, J. L. Li, A. G. Tamirat, Y. R. Liu, L. Wang, Y. G. Wang, Y. Y. Xia, *J. Mater. Chem. A* **2018**, *6*, 1443.
- [5] H. L. Pan, Y. Y. Shao, P. F. Yan, Y. W. Cheng, K. S. Han, Z. M. Nie, C. M. Wang, J. H. Yang, X. L. Li, P. Bhattacharya, K. T. Mueller, J. Liu, *Nat. Energy* **2016**, *1*, 16039.
- [6] J. M. Qian, T. T. Wang, Z. M. Zhang, Y. G. Liu, J. F. Li, D. Q. Gao, *Nano Energy* **2020**, *74*, 104948.
- [7] Y. G. Li, J. Lu, *ACS Energy Lett.* **2017**, *2*, 1370–1377.
- [8] D. X. Ji, L. Fan, L. L. Li, S. J. Peng, D. S. Yu, J. N. Song, S. Ramakrishna, S. J. Guo, *Adv. Mater.* **2019**, *31*, 1808267.
- [9] L. Zhang, J. Xiong, Y. H. Qin, C. W. Wang, *Carbon* **2019**, *150*, 475–484.
- [10] S. Chen, L. L. Zhao, J. Z. Ma, Y. Q. Wang, L. M. Dai, J. T. Zhang, *Nano Energy* **2019**, *60*, 536–544.
- [11] L. C. Diao, T. Yang, B. Chen, B. Zhang, N. Q. Zhao, C. S. Shi, E. Z. Liu, L. Y. Ma, C. N. He, *J. Mater. Chem. A* **2019**, *7*, 21232.
- [12] J. Yu, B. Q. Li, C. X. Zhao, J. N. Liu, Q. Zhang, *Adv. Mater.* **2020**, *32*, 1908488.
- [13] T. Tang, W. J. Jiang, X. Z. Liu, J. Deng, S. Niu, B. Wang, S. F. Jin, Q. Zhang, L. Gu, J. S. Hu, L. J. Wan, *J. Am. Chem. Soc.* **2020**, *142*, 7116–7127.
- [14] X. J. Zheng, X. C. Cao, K. Zeng, Z. H. Sun, J. Yan, X. W. Li, C. Jin, X. Chen, R. Z. Yang, *J. Mater. Chem. A* **2020**, *8*, 11202–11209.
- [15] F. L. Meng, H. X. Zhong, J. M. Yan, X. B. Zhang, *Nano Res.* **2017**, *10*, 4436–4447.
- [16] F. Yang, X. Q. Liu, H. Z. Zhang, J. H. Zhou, J. X. Jiang, X. H. Lu, *Energy Storage Mater.* **2020**, *30*, 138–145.
- [17] C. Y. Wang, N. H. Xie, Y. L. Zhang, Z. H. Huang, K. L. Xia, H. M. Wang, S. J. Guo, B. Q. Xu, Y. Y. Zhang, *Chem. Mater.* **2019**, *31*, 1023–1029.
- [18] Z. Q. Cao, H. B. Hu, M. Z. Wu, K. Tang, T. T. Jiang, *J. Mater. Chem. A* **2019**, *7*, 17581–17593.
- [19] Y. H. Cao, X. R. Zheng, H. X. Zhang, J. F. Zhang, X. P. Han, C. Zhong, W. B. Hua, Y. D. Deng, *J. Power Sources* **2019**, *437*, 226893.
- [20] Y.-N. Chen, X. Zhang, H. J. Cui, X. Zhang, Z. J. Xie, X. G. Wang, M. G. Jiao, Z. Zhou, *Energy Storage Mater.* **2018**, *15*, 226–233.
- [21] B. Li, K. Igawa, J. W. Chai, Y. Chen, Y. Wang, D. W. H. Fam, N. N. Tham, T. An, T. Konno, A. Q. Sng, Z. L. Liu, H. Zhang, Y. Zong, *Energy Storage Mater.* **2020**, *25*, 137–144.
- [22] Y.-B. Guo, S. Yao, L. X. Gao, A. Chen, M. G. Jiao, H. J. Cui, Z. Zhou, *J. Mater. Chem. A* **2020**, *8*, 4386–4395.
- [23] Y.-N. Chen, Y.-B. Guo, H. J. Cui, Z. J. Xie, X. Zhang, J. P. Wei, Z. Zhou, *J. Mater. Chem. A* **2018**, *6*, 9716–9722.
- [24] Y. Y. Guo, P. F. Yuan, J. N. Zhang, Y. F. Hu, I. S. Amiinu, X. Wang, J. G. Zhou, H. C. Xia, Z. B. Song, Q. Xu, S. C. Mu, *ACS Nano* **2018**, *12*, 1894–1901.
- [25] Q. Lu, Y. N. Guo, P. Mao, K. M. Liao, X. H. Zou, J. Dai, P. Tan, *Energy Storage Mater.* **2020**, *32*, 20–29.
- [26] Z. Y. Xu, X. J. Zhang, X. D. Wang, J. J. Fang, Y. F. Zhang, X. R. Liu, W. Zhu, Y. S. Yan, Z. B. Zhuang, *ACS Nano* **2021**, *15*, 7131–7138.
- [27] C. Q. Huang, Y. H. Zhong, J. X. Chen, J. Li, W. Zhang, J. Q. Zhou, Y. L. Zhang, L. Yua, Y. Yu, *Chem. Eng. J.* **2021**, *403*, 126304.

- [28] Y. Y. She, J. Liu, H. K. Wang, L. Li, J. S. Zhou, M. K. H. Leung, *Nano Res.* **2020**, *13*, 2175–2182.
- [29] B. J. Hopkins, M. B. Sassin, C. N. Chervin, P. A. DeSario, Joseph F. Parker, J. W. Long, D. R. Rolison, *Energy Storage Mater.* **2020**, *27*, 370–376.
- [30] J. Kim, O. Gwon, O. Kwon, J. Mahmood, C. M. Kim, Y. J. Yang, H. Lee, J. H. Lee, H. Y. Jeong, J. B. Baek, G. Kim, *ACS Nano* **2019**, *13*, 5502–5512.
- [31] I. S. Amiiniu, X. B. Liu, Z. H. Pu, W. Q. Li, Q. D. Li, J. Zhang, H. L. Tang, H. N. Zhang, S. C. Mu, *Adv. Funct. Mater.* **2018**, *28*, 1704638.
- [32] X. X. Wang, D. A. Cullen, Y. T. Pan, S. Hwang, M. Y. Wang, Z. X. Feng, J. Y. Wang, M. H. Engelhard, H. G. Zhang, Y. H. He, Y. Y. Shao, D. Su, K. L. More, J. S. Spendelow, G. Wu, *Adv. Mater.* **2018**, *30*, 1706758.
- [33] D. D. Zhu, M. Qiao, J. L. Liu, T. Tao, C. X. Guo, *J. Mater. Chem. A* **2020**, *8*, 8143–8170.
- [34] K. Chen, Z. H. Sun, R. P. Fang, Y. Shi, H. M. Cheng, F. Li, *Adv. Funct. Mater.* **2018**, *28*, 1707592.
- [35] D. Chen, Z. H. Pu, R. H. Lu, P. X. Ji, P. Y. Wang, J. W. Zhu, C. Lin, H. W. Li, X. G. Zhou, Z. Y. Hu, F. J. Xia, J. S. Wu, S. C. Mu, *Adv. Energy Mater.* **2020**, *10*, 2000814.
- [36] M. Kuang, Y. Wang, W. Fang, H. T. Tan, M. X. Chen, J. D. Yao, C. T. Liu, J. W. Xu, K. Zhou, Q. Y. Yan, *Adv. Mater.* **2020**, *32*, 2002189.
- [37] Y. Wang, P. Zheng, M. X. Li, Y. R. Li, X. Zhang, J. Chen, X. Fang, Y. J. Liu, X. L. Yuan, X. P. Dai, H. Wang, *Nanoscale* **2020**, *12*, 9669–9679.
- [38] J. Z. Y. Seow, T. D. Nguyen, *Electrochim. Acta* **2020**, *341*, 136058.
- [39] Q. T. Liu, Y. C. Li, L. R. Zheng, J. X. Shang, X. F. Liu, R. H. Yu, J. L. Shui, *Adv. Energy Mater.* **2020**, *10*, 2000689.
- [40] D. D. Li, H. C. Qi, H. M. Zhao, L. Ding, Z. X. Zhang, Z. Y. Guo, *Chem. Commun.* **2019**, *55*, 10092–10095.
- [41] H. H. Lv, X. B. Zhang, F. M. Wang, G. J. Lv, T. T. Yu, M. L. Lv, J. W. Wang, Y. Zhai, J. Q. Hu, *J. Mater. Chem. A* **2020**, *8*, 14287–14298.
- [42] S. H. Zhang, W. Xia, Q. Yang, Y. V. Kaneti, X. T. Xu, S. M. Alshehri, T. Ahamad, M. S. A. Hossain, J. Nae, J. Tang, Y. Yamauchi, *Chem. Eng. J.* **2020**, *396*, 125154.
- [43] H. C. Qi, Y. Y. Feng, Z. Z. Chi, Y. Y. Cui, M. H. Wang, J. Liu, Z. Y. Guo, L. Wang, S. H. Feng, *Nanoscale* **2019**, *11*, 21943.
- [44] C. Hang, J. Zhang, J. W. Zhu, W. Q. Li, Z. K. Kou, Y. H. Huang, *Adv. Energy Mater.* **2018**, *8*, 1703539.
- [45] M. J. Yang, X. H. Hu, Z. S. Fang, L. Sun, Z. K. Yuan, S. Y. Wang, W. Hong, X. D. Chen, D. S. Yu, *Adv. Funct. Mater.* **2017**, *27*, 1701971.
- [46] W. Xia, J. H. Zhu, W. H. Guo, L. An, D. G. Xia, R. Q. Zou, *J. Mater. Chem. A* **2014**, *2*, 11606–11613.
- [47] F. L. Meng, H. X. Zhong, D. Bao, J. M. Yan, X. B. Zhang, *J. Am. Chem. Soc.* **2016**, *138*, 10226–10231.

Manuscript received: August 16, 2021

Revised manuscript received: September 26, 2021

Version of record online: October 29, 2021